Experimental and Theoretical Characterization of Sonochemical Cells. Part 1. Cylindrical Reactors and Their Use to Calculate the Speed of Sound in Aqueous Solutions

Peter R. Birkin,*,† Timothy G. Leighton,‡ John. F. Power,† Matthew D. Simpson,‡ Aurore M. L. Vinçotte,† and Phillip F. Joseph‡

Department of Chemistry, University of Southampton, Southampton, SO17 1BJ, United Kingdom, and Institute of Sound and Vibration Research, University of Southampton, Southampton, SO17 1BJ, United Kingdom

Received: December 13, 2001; In Final Form: August 22, 2002

The sound field generated from a cylindrical sonochemical cell is discussed in depth. This sound field is considered with a variable operating frequency. An acoustic model is developed to predict the spatial distribution of acoustic pressure, which is compared with experimental measurements of the spatial characteristics of luminescent emission from a cylindrical cell. A sound speed (averaged in space and time) within the cavitation environment in the range of 868−1063 m s^{-1} was calculated. Under certain assumptions, this corresponds to a void fraction range of 2.9×10^{-3} to 4.2×10^{-3}%. The implications for electrochemical and chemical activity within cylindrical cells are discussed.

Introduction

Cavitation, generated within a reactor, can be used to drive a range of physical and chemical processes. These processes include the disruption of algae growths, the processing of food materials, the acceleration of chemical reactions, the modification of surfaces, and the reduction of polymer molecular weights.[1−9] However, it is clear that in order to understand fully and hence exploit the beneficial effects of cavitation, it is necessary to characterize the acoustics of the reactors or cells employed in these experiments. Cavitation is most widely generated through the use of high power ultrasound, although other generation methods such as flow have been demonstrated to be chemically useful.[10] In the case of sonochemical exploitation, little or no attention has been given to the understanding of acoustics of ultrasonic reactors in relation to the spatial characteristics and performance of the chemical experiments performed within these acoustic cells. This is unfortunate but may be the result of an insufficiently interdisciplinary approach encompassing the different scientific fields underlying the chemical and physical natures of the science. In this paper, a discussion on the merits of addressing the acoustics of a sonochemical cell is suggested.

Difficulties in the interpretation of experimental results found in the literature, obtained from sonochemical experiments, are compounded by the wide variety of different frequencies and experimental conditions under which they were performed. This applies to the set of sonoelectrochemical experiments.[11−20] However, most of these experiments have been performed with ultrasonic probes, which generate high intensity localized cavitation but are usually restricted to the lower frequency range around 20 kHz. The sound fields generated from these types of ultrasonic sources and the consequences to chemistry within this type of environment are discussed elsewhere.[21] In general, the source of ultrasound used in sonochemical experiments has been of fixed frequency but is most commonly in the 20−1000 kHz range. In many instances, it may be impractical to employ cell disrupter sound sources to perform useful chemical or physical work. A common experience with many would be the immersion of an apparatus within an ultrasonic cleaning bath or reaction vessel. In this operation, cavitation action is required over a large volume and so a spatially extensive sound field is employed, instead of a concentrated sound field such as that produced by ultrasonic horn type sources.

Trablesi et al. were among the first to study, using an electrochemical approach, the effects of high (561 kHz) frequency ultrasound within a cylindrical cell. They reported the effect of ultrasound at 561 kHz on mass transfer of material to an electrode surface.[22] Trablesi et al. reported that mass transfer activity was highest off axis in a ringlike pattern within the cell. In a later investigation, Compton et al. reported the effects on mass transfer and surface erosion of 500 kHz ultrasound produced within a cylindrical electrochemical cell.[23] These authors commented that under certain conditions, a circular pattern of highest mass transfer within their cell was observed in agreement with the pattern reported by Trablesi et al. Other electrochemical studies have shown the presence of streamers (well-known from visual observations of cavitation clouds[24−26]) within cylindrical cells operating below 100 kHz. Clearly, many interesting results obtained from these electrochemical studies[27,28] are, as yet, not fully understood.

To characterize the sound field generated within the sonochemical reactor, it is necessary to employ a technique that has the ability to spatially resolve cavitation activity (or the associated effects of cavitation) within the reactor. This is achieved here by employing a photographic technique involving a sonochemiluminescent reaction. This reaction, specifically the oxidation of luminol[29−32] (tri-aminophthalhydrazine) by oxidants produced by cavitation (usually assumed to be $OH^{\bullet}$),[31] was recorded using an image-intensified camera within a dark room. As is common in multiple bubble fields, this technique is assumed to be sensitive to the generation of radical species, which are known to result from cavitation.[33−37]

In this paper, the sound field from a reactor with a cylindrical geometry is discussed. The sound field generated by this reactor

* To whom correspondence should be addressed. Fax: +44(0)2380 593781. E-mail prb2@soton.ac.uk.
† Department of Chemistry, University of Southampton.
‡ Institute of Sound and Vibration Research, University of Southampton.

10.1021/jp014532t CCC: $25.00
Published on Web 12/14/2002

will be discussed in terms of the cavity acoustic modes.[38] The consequences of the acoustics of this cell on the electrochemical and sonochemical results are discussed in relation to the previous literature relevant to this topic.

Experimental Section

Apparatus. Images of the light emission patterns within the cells employed were recorded within a dark room. A Darkstar intensifier CCD camera (Photonic Science) with a Nicam video recorder was employed to record and capture the images, respectively.

Two cylindrical cells were employed. The exact dimensions and construction of these cells are given in the figure legends. Each cell was attached to a sandwich transducer (Morgan Electro Ceramics Ltd.) with epoxy resin (Struers, Epofix). In most cases, a water-jacketed system was employed to maintain temperature control. This cell had a sandwich transducer with a resonance frequency ca. 27 kHz, transducer properties[39] (air) Q factor 900 ± 200, resonant impedance 15 ± 5 ohms, effective coupling coefficient 0.37 ± 0.02, and shunt capacitance 3.7 nF. The single-walled cell (e.g., Figures 3 and 9) had a sandwich transducer (Morgan Electro Ceramics Ltd.) with a resonance frequency of ca. 33 kHz (resonant impedance 5−15 ohms, effective coupling coefficient 0.36−0.38, and shunt capacitance 6.7−7.3 nF).[39] A programmable function generator (Thurlby Thandar Instruments, TG1010) was used to generate a signal at the required frequency. The signal was amplified (Brüel & Kjaer 2713 power amplifier) before driving the transducer. The postamplification voltage (zero to peak) across the transducer was reported in the appropriate figure legend. This voltage was measured using a Tektronix TDS 224 oscilloscope.

Pressure amplitude measurements (shown in parentheses in figure legends 3−6, 11) were performed using a Brüel & Kjaer 8103 calibrated hydrophone (Note that due to the finite size of the active element the spatial maximum zero-to-peak pressure amplitudes cited in the captions will be underestimates because of spatial averaging.[44,49]) and Brüel & Kjaer 2635 charge amplifier. The output was recorded on a Tektronix TDS 224 oscilloscope and converted into pressure using the calibration figures provided by the hydrophone manufacturer. Because of the alkali nature of the sonochemiluminescent media (which could be detrimental to the hydrophone housing), a 100 mmol dm^{-3} Na_2SO_4 solution was employed in these pressure measurements. For each particular frequency employed, the hydrophone was moved within the cell using a XYZ micrometer and stage until the maximum pressure was found. Further pressure measurements at the same frequency and in the same cell, temperature, and volume were measured in this position. These pressure measurements are included in parentheses in the appropriate figure legend.

To measure the spatial variation of the sound field in the cavity in the absence of cavitation, a GRAS 10 CF hydrophone was employed. This was positioned in the cell and moved with a micrometer and stage (travel 25 mm, resolution 10 μm). The output was recorded on a Tektronix TDS 224 oscilloscope. Sound speed measurements, in the absence of cavitation, were undertaken by monitoring the propagation delay time at a GRAS 10 CF hydrophone as a function of distance in the axial z direction. A pulsed signal was generated by applying a voltage step (−5 to 5 V) to the transducer. To reduce complications due to the cell wall reflection, the distance between the hydrophone and the cell base was always less than the distance between the cell wall and the hydrophone. The distance dependence of the propagation delay time of the hydrophone enabled the speed of sound within the media to be estimated independent of the transducer and hydrophone response times. To minimize the bubble population within the solution (see Figure 8, ○), the liquid was filtered (0.22 μm) and then degassed under vacuum for 30 min. The solution was then carefully decanted into the sonochemical cell.

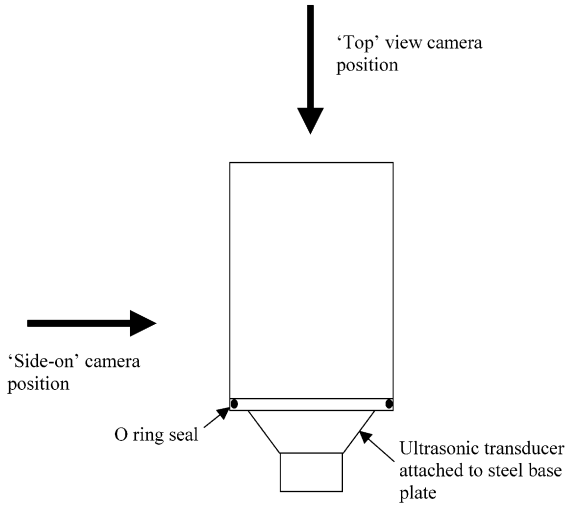

Figure 1. Diagram showing a schematic demonstrating the orientation of the camera with respect to the single-walled Perspex cell. The cell was constructed using a Perspex cylinder and a stainless steel plate for the base. The seal between the wall and the base was maintained by an O-ring. This cell was used for the results shown in Figure 3 and Figure 9.

Chemicals. Aqueous solutions were prepared with water from an Elga Elect 5 or Vivendi Purelab Option 10 water purification system. The conductivity of water purified in this manner was in the range of 0.2−0.06 μS cm^{-1}. The water purified in this manner would normally stand for prolonged periods within the water system. Luminol (tri-aminophthalhydrazine, Aldrich, 97%), sodium carbonate (BDH, 99.5%), hydrogen peroxide (29−31% by mass, BDH), sodium sulfate (BDH, AnalaR, 99%) and ethylenediaminetetraacetic acid (EDTA, Lancaster Synthesis) were used as received. The concentrations of the constituents within the cell are reported in the appropriate figure legend. The ultrasonically induced emission of light was imaged using an intensified camera from above the cell or at the side. These experiments were performed in a dark room. Figure 1 shows the experimental orientation of the camera and cell.

Results and Discussion

Theory—Sound Fields Generated from Cylindrical "Cell" Configurations. To discuss the sound field generated within a cell arrangement, it is important to consider the geometry of the sound field under consideration. In this particular example, a cylindrical cell was chosen as our model system. However, other geometries could be considered using a similar approach to the one presented below.

A sound field in an enclosed cylindrical cavity can be decomposed into its natural modes. Consider a cylinder standing on a flat base. There will be modes entirely in the axial (here the vertical) direction. There will also be entirely transverse modes, some of which will have rotational symmetry about the axis (i.e., no azimuth variation) and some that will not. Summed appropriately, they will combine to produce the spatial variation of the sound field within the cylinder. Initially, however, the nature of azimuthal and radial modes will be examined separately.

We now discuss the characteristics of these acoustic modes as this will assist in the interpretation of the sonochemiluminescence plots presented subsequently.

The homogeneous acoustic wave equation is given by eq 1[38]

$$\nabla^2 p - (1/c^2)\,(\partial^2 p/\partial t^2) = 0 \tag{1}$$

where p represents the acoustic pressure, c is the speed of sound, t is time, and r, θ, and z represent the cylindrical coordinate system. In a cylindrical coordinate system (r,θ,z), we seek separable, harmonic solutions to eq 1 of the form of eq 2.

$$p(r,\theta,z,t) = \Theta(\theta)\,R(r)\,Z(z)\,e^{i\omega t} \tag{2}$$

where Θ, R, and Z are independent functions of θ, r, and z, respectively. When the operator ∇^2 is expressed in cylindrical coordinates,[40] general solutions to eq 1 are obtained of the form

$$\Theta(\theta) = e^{im\theta} \tag{3}$$

$$R(r) = b_1\,J_m(k_r r) + b_2\,Y_m(k_r r) \tag{4}$$

$$Z(z) = b_3 \sin(k_z z) + b_4 \cos(k_z z) \tag{5}$$

where b_1, b_2, b_3, and b_4 represent constants, $J_m(k_r r)$ and $Y_m(k_r r)$ are Bessel functions of the first and second kind, respectively, of order m, where m is confined to integer values to ensure periodicity of the solution in the θ direction. Substituting eqs 3−5 into eq 1 shows that transverse and axial wavenumbers k_r and k_z are coupled via

$$k_z^{\,2} + k_r^{\,2} = k^2 \tag{6}$$

The wavenumbers k_r and k_z are determined from the boundary conditions at the vessel walls. The water−air boundary at $z = 0$ is, to a good approximation, pressure release, such that $Z(0) = 0$. The base of the cell at $z = L$ is regarded as a rigid boundary, such that the axial particle velocity is zero and hence $\partial Z(z)/\partial z|_{z=L} = 0$. These boundary conditions preclude the cosine term in eq 5 as a possible solution. The infinite set of axial wavenumber k_{zq} that satisfies these boundary conditions is given by eq 7.

$$k_{zq} = [(2q + 1)\pi/2L] \tag{7}$$

where q takes the integer values (0, 1, 2...).

The boundary condition at the curved walls is potentially more complicated. Even with a single glass wall, the acoustic wave encounters a water/glass/air interface, and the existence of a water jacket makes this more complicated. Appendix A presents a rigorous calculation of the reflection coefficients of two such walled cells. Appendix A shows that the phase angle (ϕ) on reflection is nonzero. However, the correction factor (also shown in Appendix A) is small (<5.5%) and as such can be ignored. Hence, to a first approximation and within a certain frequency range, the inner surface of the innermost glass wall approximates to a rigid boundary. Hence, the appropriate boundary conditions in the radial direction at $r = a$ are

$$\partial R(r)/\partial r|_{r=a} = 0 \tag{8}$$

These boundary conditions preclude the possibility of Y_m in eq 3 as a possible solution. Equation 8 restricts possible k_r values to those for which $\partial J_m(k_{rmn} r)/\partial r|_{r=a} = 0$ so that k_{rmn} is given by eq 9.

$$k_{rmn} = [j_{mn}/a] \tag{9}$$

where j_{mn} is the nth stationary value of the Bessel function of the first kind of order m and a is the inner cylinder radius.

Combining eqs 3−5 and omitting the time dependence, the spatial variation of acoustic pressure in the vessel at a single frequency may be expressed in the form

$$p(r,\theta,z) = \sum_{m=-\infty}^{\infty} \sum_{n=0}^{\infty} \sum_{q=0}^{\infty} A_{mnq}\,e^{im\theta}\,J_m[k_{rmn} r] \sin(k_{zq} z) \tag{10}$$

where A_{mnq} represents the amplitude of the (m,n,q)th mode, and m, n, and q are the modal integers denoting the azimuthal, radial, and axial mode integers, respectively.

If, for example, the driving system is axisymmetric, then the resultant sound field may be considered to be axially symmetric. There is no θ dependence, and the θ term may be ignored. If this is the case, then we restrict ourselves to a zero order Bessel function for which $m = 0$. Hence, we are left to consider the r and z terms and eq 10 reduces to

$$p(r,z) = \sum_{n=0}^{\infty} \sum_{q=0}^{\infty} A_{0nq}\,J_0[k_{r0n} r] \sin(k_{zq} z) \tag{11}$$

From eqs 6, 7, and 9, the natural resonance frequency f_{0nq} of the $(0,n,q)$th cavity mode is given by

$$f_{0nq} = (c/2\pi)\,\{(j_{0,n}/a)^2 + [(2q + 1)\pi/2L]^2\}^{1/2} \tag{12}$$

Equation 11 is plotted for the $q = 6$, $n = 5$, and $m = 0$ mode in Figure 2. The horizontal pattern corresponds to a central maximum ("spot" as viewed from above) and rings of local maxima in the radial direction. If the spatially averaged sound speed is known, then it is possible to use this model to predict natural frequencies of the modes (it should be noted that damping would impart to a given mode a finite bandwidth about its natural frequency). To do this, one needs to know the dimensions of the vessel and the spatially averaged sound speed in the liquid. The latter requirement demonstrates one of the most important findings of this paper, because when acoustic fields are calculated for sonochemical studies (which is rare) the sound speed of bubble free water is assumed (e.g., ca. 1500 m s^{-1}). The actual sound speed in bubbly water in a reaction vessel is calculated in this paper. Table 1 shows the frequencies of the first few axisymmetric modes for a reaction vessel, calculated using sound speeds of 1500 (bubble free water) and 1000 m s^{-1} (a bubbly mixture).

If, however, departures from axisymmetry occur (for example, if the driving transducer is not totally symmetric in nature), then we must consider higher order Bessel functions. As a result, the θ variation of the resultant sound field becomes apparent. In this case, it is appropriate to use eq 13 to predict the mode frequency.

$$f_{m,n,q} = (c/2\pi)\,\{(j_{m,n}/a)^2 + [(2q + 1)\pi/2L]^2\}^{1/2} \tag{13}$$

The horizontal pattern of the sound field now can include a series of rings split by the θ dependence in the radial direction with bands in the axial direction. Table 2 shows the values of $j_{m,n}$ for a rigid boundary at the inner interface (see Appendix A). This model predicts that the integer values of m, n, and q will be involved in the calculations of the natural frequencies, and as such, a three-dimensional table is appropriate. However,

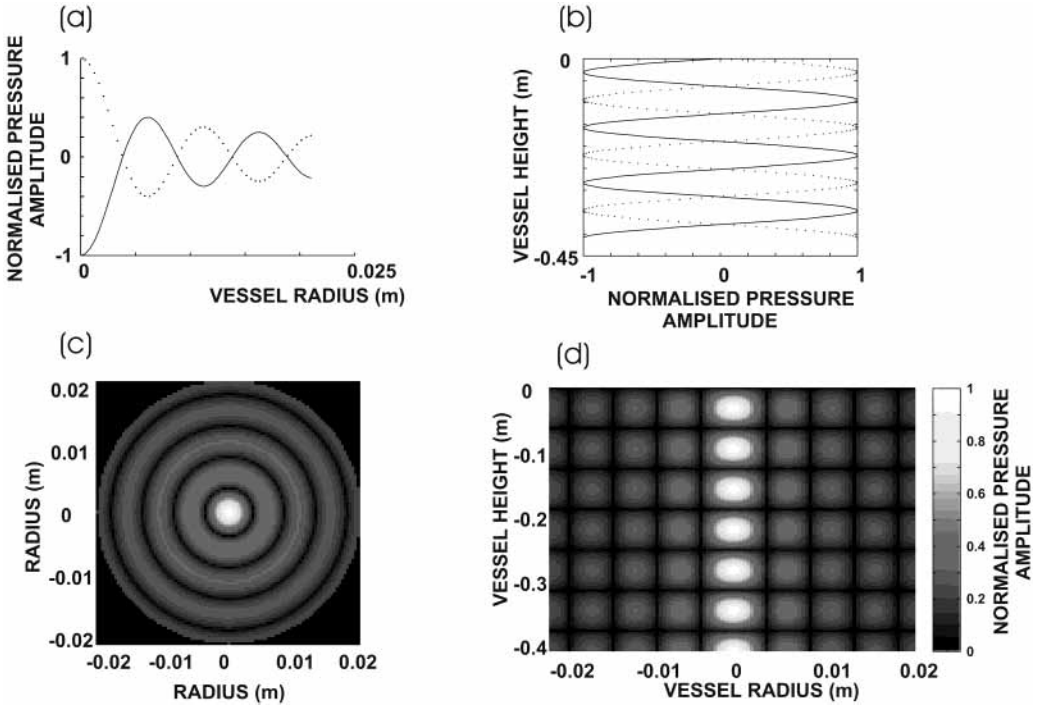

Figure 2. Four plots describing the calculated reverberant pressure amplitude within a cylindrical cell. Verification of the model is found in the pressure release and rigid characteristics at the $z = 0$ and $z = L$ positions. Panel a shows the normalized pressure amplitude of panel c from the center of the vessel to the vessel wall. The maximum value at $r = 0$ is an artifact of the zero order Bessel function used to describe the reverberant radial acoustic field. Panel b shows the normalized pressure amplitude along the vertical axis of the acoustic vessel presented in panel d. Note that panels b and a represent the extremes of pressure; hence, the solid and dashed lines occur 180° out of phase.

TABLE 1: Lowest Few Natural Frequencies in kHz of the Modes of a Cylindrical Cell Calculated Using Eq 12[a]

	n					
q	2	3	4	5	6	7
0	32.00	58.01	83.95	109.93	135.76	161.59
	(21.34)	(38.67)	(55.97)	(73.29)	(90.51)	(107.73)
1	34.99	59.70	85.14	110.84	136.49	162.21
	(23.33)	(39.80)	(56.76)	(73.89)	(91.00)	(108.14)
2	40.30	62.97	87.45	112.63	137.95	163.44
	(26.87)	(41.98)	(58.30)	(75.08)	(91.97)	(108.96)
3	47.16	67.56	90.82	115.26	140.11	165.26
	(31.44)	(45.04)	(60.55)	(76.84)	(93.41)	(110.18)
4	54.99	73.24	95.12	118.68	142.93	167.67
	(36.66)	(48.83)	(63.41)	(79.12)	(95.29)	111.78
5	63.44	79.78	100.24	122.82	146.39	170.62
	(42.29)	(53.19)	(66.83)	(81.88)	(97.59)	(113.75)
6	72.28	86.98	106.06	127.61	150.43	174.10
	(48.19)	(57.98)	(70.70)	(85.07)	(100.29)	(116.07)
7	81.39	94.68	112.46	132.98	155.02	178.08
	(54.26)	(63.12)	(74.98)	(88.66)	(103.34)	(118.72)
8	90.69	102.78	119.37	138.87	160.09	182.52
	(60.46)	(68.52)	(79.58)	(92.58)	(106.73)	(121.68)

[a] The cell had a radius to the inner wall of ca. 2.9 cm and a liquid height of 7.5 cm. The integers *n* correspond to the axial order of the mode. Note that in this case $n \neq 1$ is a consequence of the boundary condition at the cell wall ($\partial J_{m,n}/\partial r = 0$). This implies that the first available mode will have to have a pressure maximum at the wall (ring) and a pressure maximum in the center of the cell (spot). For each mode, two frequencies are shown. The upper corresponds to a spatially averaged sound speed of 1500 m s^{-1} (bubble free water). The lower, in brackets, corresponds to 1000 m s^{-1} (i.e., possible for bubbly water).

if we assume a value of *q*, it is possible to predict values of the natural frequencies of a complete cylindrical cell. Table 3 shows the values of the natural frequencies assuming $q = 29$ (a value chosen from the results shown in Figure 3f). The number of rings, spots, and bands can be calculated with the formulas shown in Table 4.

TABLE 2: Values of $j_{m,n}$ at $\partial J_{m,n}/\partial r = 0$ for Zero and Higher Order Modes

	n						
m	1	2	3	4	5	6	7
0	–	3.84	7.02	10.18	13.34	16.48	19.62
1	1.86	5.34	8.54	11.72	14.88	18.02	21.18
2	3.06	6.72	9.98	13.18	16.36	19.52	22.68
3	4.22	8.02	11.36	14.6	17.8	20.98	24.16
4	5.32	9.3	12.7	15.98	19.2	22.42	25.6
5	6.42	10.52	14	17.32	20.58	23.82	27.02
6	7.52	11.74	15.28	18.64	21.94	25.2	28.42
7	8.58	12.94	16.54	19.96	23.28	26.56	29.8
8	9.66	14.12	17.78	21.24	24.6	27.9	31.16
9	10.72	15.3	19.02	22.52	25.9	29.22	32.52
10	11.78	16.46	20.24	23.78	27.18	30.54	33.86

Experimental Verification—Cylindrical Cell Geometry. To verify the acoustic model presented here, a number of experiments were performed. In each case, a cylindrical cell was employed containing a luminol solution (the exact constituents of which are shown in the appropriate figure legend). The ultrasonically induced emission of light (sonochemiluminescence) is imaged in Figures 3–6 viewed from either above or from the side of the cell (see Figure 1).

Figure 3a–e shows pictures taken from above a cylindrical cell, while frames f–i show pictures taken from the side of the same cell. In this case, the acoustic frequency is kept constant at 132.44 kHz. However, the voltage applied to the transducer is reduced from an amplitude of 106 to 57 V in steps reported in the appropriate legend (note that frames a and b are recorded under identical conditions except for a lower intensifier gain for frame b). Figure 3 shows that as the power is reduced the emission of light from the cell becomes concentrated in the center of the cell. Finally, frame e shows a single bright spot in the center of the cell. Table 5 shows the measurements made from frame b of the position of the rings within the cell. It is

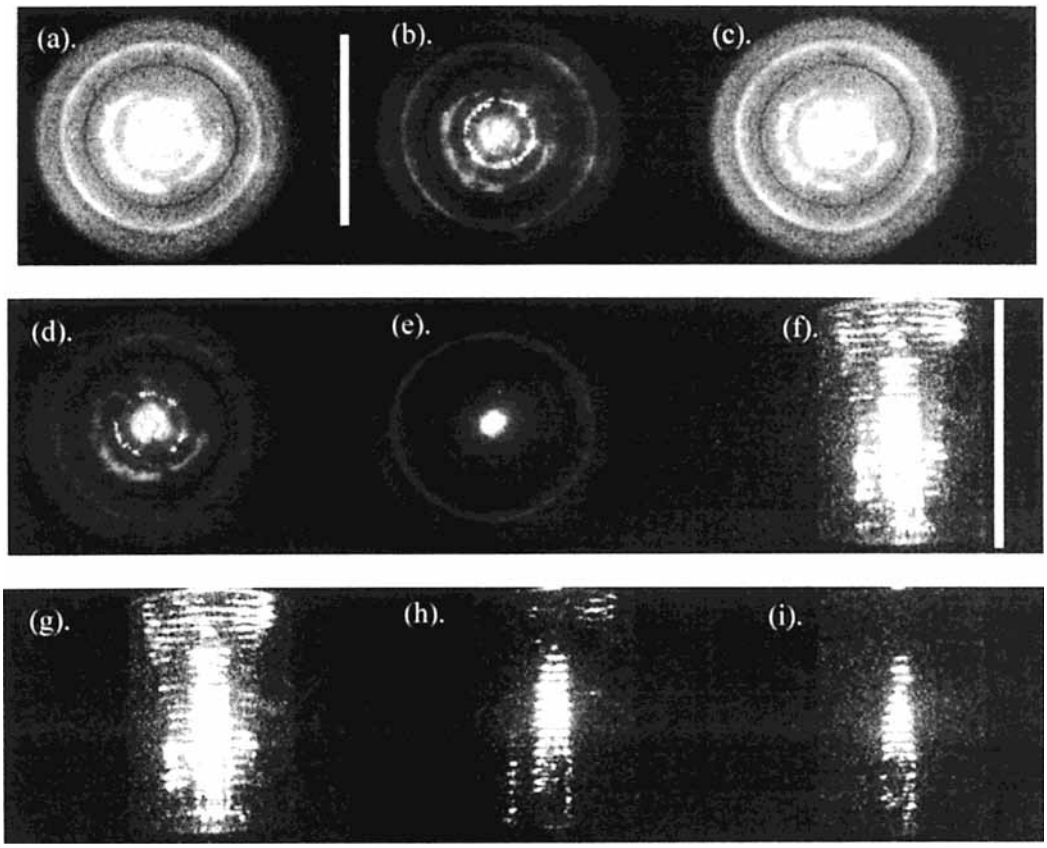

Figure 3. Frames showing the light emission from a cylindrical single-walled cell (9.4 cm internal diameter, 10 cm external diameter) recorded from above (frames a−e) and to the side (frames f−i). In all cases, the driving frequency was maintained at 132.44 kHz. The cell contained an aqueous solution of 50 μmol dm^{-3} luminol, 0.1 mmol dm^{-3} EDTA, 0.1 mmol dm^{-3} H_2O_2, and 100 mmol dm^{-3} Na_2CO_3. The pictures were recorded under ambient conditions (ca. 20−23 °C) in aerobic media. The solution height was maintained at 14 cm. The applied voltage was 106 V (0.75 bar) for frames a, b, and f; 95 V (0.62 bar) for frames c and g; 83 V (0.51 bar) for frames d and h; and 57 V (0.44 bar) for frames e and i. The scale bar in frame a represents 9.4 cm and applies to frames a−e while the scale bar in frame f represents 14 cm and applies to frames f−i. See parenthetical note in the Experimental Section.

possible to estimate from frame f that there are 30 bands of light. This corresponds to $q = 29$ (see Table 4).

At this point, it must be remembered that the presence of bubbles within the liquid can perturb the speed of sound within the media. The effective speed of sound can either be greater or less than the value for bubble free water (assumed here to be 1500 m s^{-1}) depending on the size distribution and applied ultrasonic frequency. As an example, Fox et al. reported speeds of sound in the range of 500−2500 m s^{-1} in bubbly liquids.[41] Bubbles that have a resonant frequency below (e.g., having radii larger than that of resonance bubbles) the applied ultrasonic frequency tend to raise the speed of sound, while bubbles with a higher resonant frequency (e.g., having radii smaller than that of resonance bubbles) tend to reduce the speed of sound. If both types are present, the net result can still be calculated. The modes determined by the photographic evidence can be combined with eqs 12 or 13 (depending on the particular case) to determine the actual sound speed within the cell. As an example, Figure 3 shows a $(m,n,q) = (0,7,29)$ mode (identified by counting rings, etc. after Table 4). The assignment and measurement of the ring spacing are shown in Table 5. Employing eq 12 and a sound speed of 1500 m s^{-1} (bubble free liquid) would predict a mode frequency of 186.9 kHz. The fact that the driving frequency to obtain this mode was 132.44 kHz allows us to estimate that the speed of sound has been reduced to $1500 \times 132.44/186.9 = 1062$ m s^{-1} within the bubbly liquid within the cell. Further evidence for the effects of bubbles on the speed of sound can be gathered by observing other modes within a cylindrical cell.

TABLE 3: Frequencies in kHz Corresponding to the $(2q + 1) = 59$ System[a]

	n						
m	1	2	3	4	5	6	7
0		159.24	162.03	166.31	172.01	178.92	186.95
		(106.16)	(108.02)	(110.88)	(114.67)	(119.28)	(124.63)
1	158.32	160.36	163.91	168.92	175.25	182.73	191.31
	(105.55)	(106.90)	(109.27)	(112.61)	(116.83)	(121.82)	(127.54)
2	158.80	161.70	166.00	171.67	178.63	186.68	195.71
	(105.87)	(107.80)	(110.67)	(114.46)	(119.09)	(124.45)	(130.47)
3	159.49	163.22	168.28	174.64	182.17	190.74	200.25
	(106.33)	(108.82)	(112.19)	(116.43)	(121.45)	(127.16)	(133.50)
4	160.34	164.97	170.75	177.74	185.81	194.93	204.83
	(106.89)	(109.98)	(113.83)	(118.49)	(123.88)	(129.96)	(136.55)
5	161.38	166.86	173.36	180.96	189.60	199.19	209.50
	(107.59)	(111.24)	(115.57)	(120.64)	(126.40)	(132.79)	(139.67)
6	162.61	168.96	176.14	184.33	193.51	203.54	214.25
	(108.40)	(112.64)	(117.43)	(122.89)	(129.01)	(135.70)	(142.83)
7	163.96	171.21	179.06	187.88	197.53	207.97	219.05
	(109.31)	(114.14)	(119.38)	(125.25)	(131.69)	(138.65)	(146.04)
8	165.51	173.61	182.12	191.48	201.63	212.47	223.90
	(110.34)	(115.74)	(121.41)	(127.65)	(134.42)	(141.65)	(149.27)
9	167.19	176.18	185.33	195.23	205.81	217.02	228.86
	(111.46)	(117.46)	(123.56)	(130.16)	(137.20)	(144.68)	(152.57)
10	169.03	178.87	188.65	199.07	210.04	221.68	233.84
	(112.69)	(119.25)	(125.77)	(132.71)	(140.03)	(147.79)	(155.89)

[a] These frequencies were calculated by employing eq 13, $a = 4.7$ cm, $L = 14$ cm. For each mode, two frequencies are shown. The upper corresponds to a spatially averaged sound speed of 1500 m s^{-1} (bubble free water). The lower, in brackets, corresponds to 1000 m s^{-1} (i.e., possible for bubbly water).

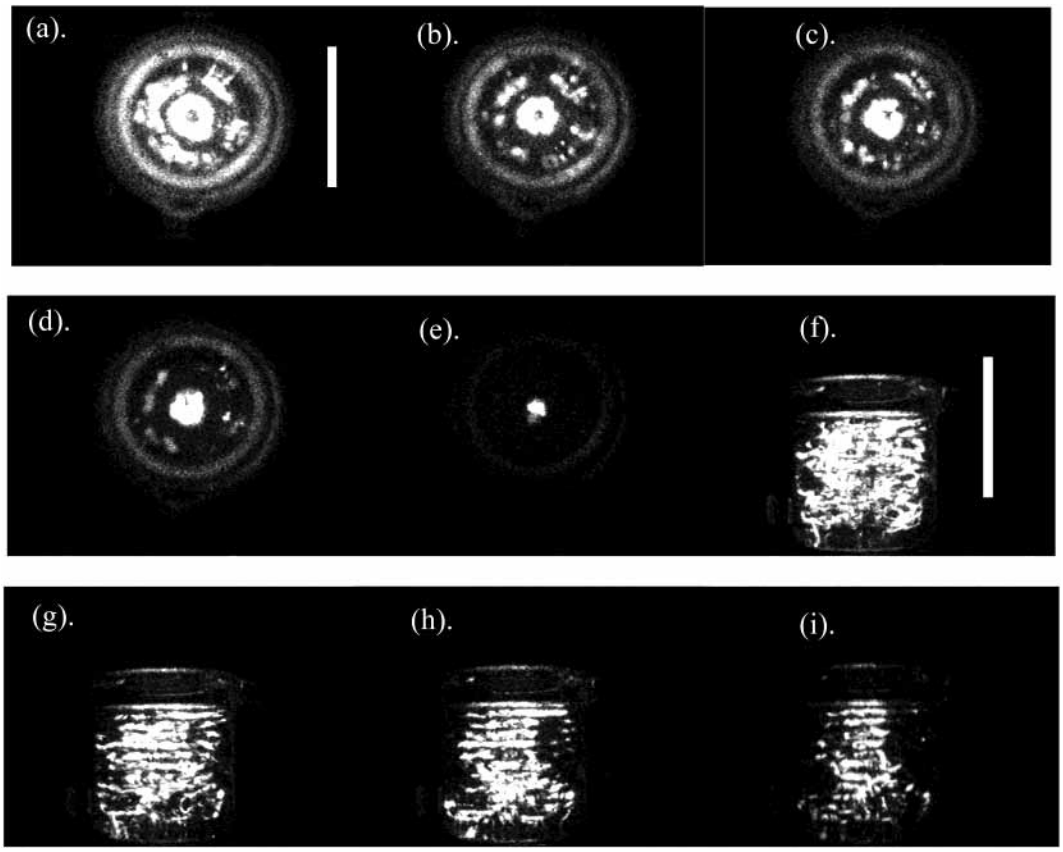

Figure 4. Frames showing the light emission from a cylindrical double-walled cell (5.8 cm internal diameter, 8.5 cm external diameter, and height 12 cm) recorded from above (frames a−e) and from the side (frames f−i). In all cases, the driving frequency was maintained at 125.23 kHz. The cell contained an aqueous solution identical to that reported in the legend of Figure 3. The cell was jacketed at 25 °C under aerobic conditions. The applied voltage was 110 V (2.58 bar) for frames a and f, 96 V (1.84 bar) for frames b and g, 80 V (1.40 bar) for frames c and h, and 60 V (0.92 bar) for frames d and i, and 30 V (0.76 bar) for frame e. The scale bar in frame a represents 5.8 cm and applies to frames a−e while the scale bar in frame f represents 7.5 cm and applies to frames f−i. See parenthetical note in the Experimental Section.

TABLE 4: Variables Discussed in the Acoustic Model Described in the Text and the Experimental Consequences of Each Variable on the Patterns of Luminescence (Assuming that Bright Luminecsence Is Associated with Spatial Maxima in Acoustic Pressure)

model parameter	experimental consequence for observation of luminescence
$q = 0, 1, 2...$	$(q + 1)$ bands in z direction (including a band at the base).
$m = 0$	Axially symmetric mode. Zero order Bessel function implies a central spot followed by rings when the cell is viewed from above (see Figure 1).
$m = 1, 2, 3....$	Nonaxially symmetric system. Higher order Bessel function implies no central spot but a series of rings when the cell is viewed from above (see Figure 1). The $m \neq 0$ assignment also implies that the rings are sliced into $2m$ segments.
$n = 1, 2, 3.....$	Number of rings and spot ($m = 0$, $n \neq 1$) or rings ($m > 0$, $n = 1, 2, 3...$) when the cell is viewed from above (see Figure 1).

Figure 4a−e shows pictures of a glass-jacketed cylindrical cell recorded from above while frames f−i show pictures taken from the side. Again, clear evidence for rings can be seen in the images. However, in addition, a central dark spot was observed. Given that the modal bandwidth at this frequency suggests that only one mode is excited, it is a nonaxisymmetric mode. Measurement of the spacing of the rings and comparison to the model identifies it as the (3,4,5) mode. The assignment and measurement of the ring spacing are shown in Table 6. Again, the natural frequency of this mode predicted for $c =$ 1500 m s^{-1} (196.14 kHz) is higher than the actual driving frequency (125.23 kHz), indicating a reduced sound speed due to the presence of bubbles within the liquid ($1500 \times 125.23/196.14 = 958$ m s^{-1}).

TABLE 5: Measured and Predicted Ring Spacing for the Data Shown in Figure 3

	measured distance (cm)	predicted distance (cm)
ring 1	0.72 ± 0.2	0.9
ring 2	1.67 ± 0.2	1.66
ring 3	2.70 ± 0.2	2.45
m,n		0,7
$j_{m,n}$		19.62
$f_{0,7,29}^{\text{natural}}$ (kHz)[a]		186.8

[a] These values were calculated using the assignment system reported in Table 4 and a sound speed of 1500 m s^{-1}.

TABLE 6: Measured and Predicted Ring Spacing for the Data Shown in Figure 4

	measured distance (cm)	predicted distance (cm)
ring 1	0.84 ± 0.2	0.85
ring 2	1.68 ± 0.2	1.60
ring 3	2.31 ± 0.2	2.25
m,n		3,4
$j_{m,n}$		14.60
$f_{3,4,15}^{\text{natural}}$ (kHz)[a]		196.14

[a] These values were calculated using the assignment system reported in Table 4 and a sound speed of 1500 m s^{-1}.

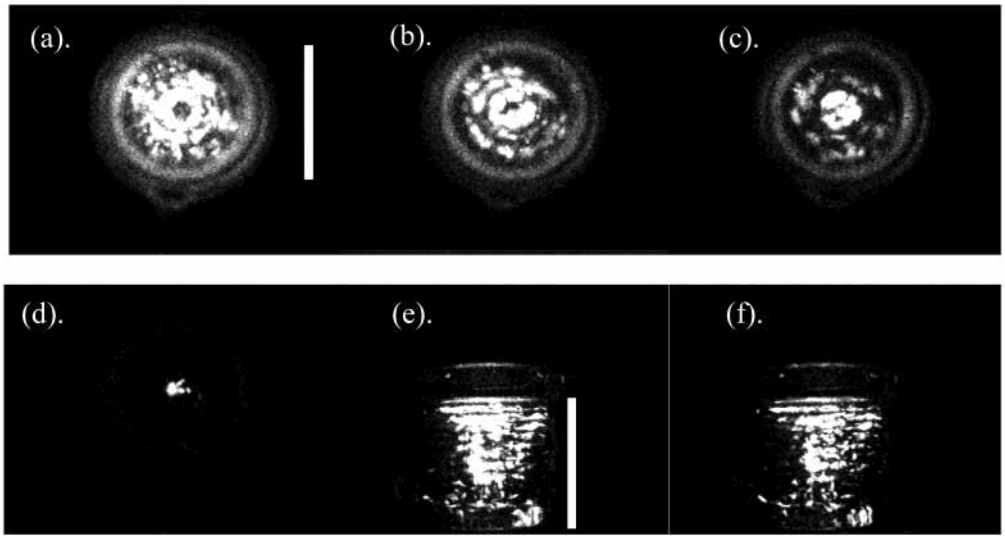

Figure 5. Frames showing the light emission from a cylindrical double-walled cell (5.8 cm internal diameter, 8.5 cm external diameter, and height 12 cm) recorded from above (frames a−d) and from the side (frames e and f). In all cases, the driving frequency was maintained at 121.83 kHz. The cell contained an aqueous solution identical to that reported in the legend of Figure 3. The cell was jacketed at 25 °C under aerobic conditions. The applied voltage was 110 V (2.12 bar) for frames a and e, 96 V (1.58 bar) for frames b and f, 80 V (1.22 bar) for frame c, and 30 V (0.61 bar) for frame d. The scale bar in frame a represents 5.8 cm and applies to frames a−d while the scale bar in frame e represents 7.5 cm and applies to frames e and f. See parenthetical note in the Experimental Section.

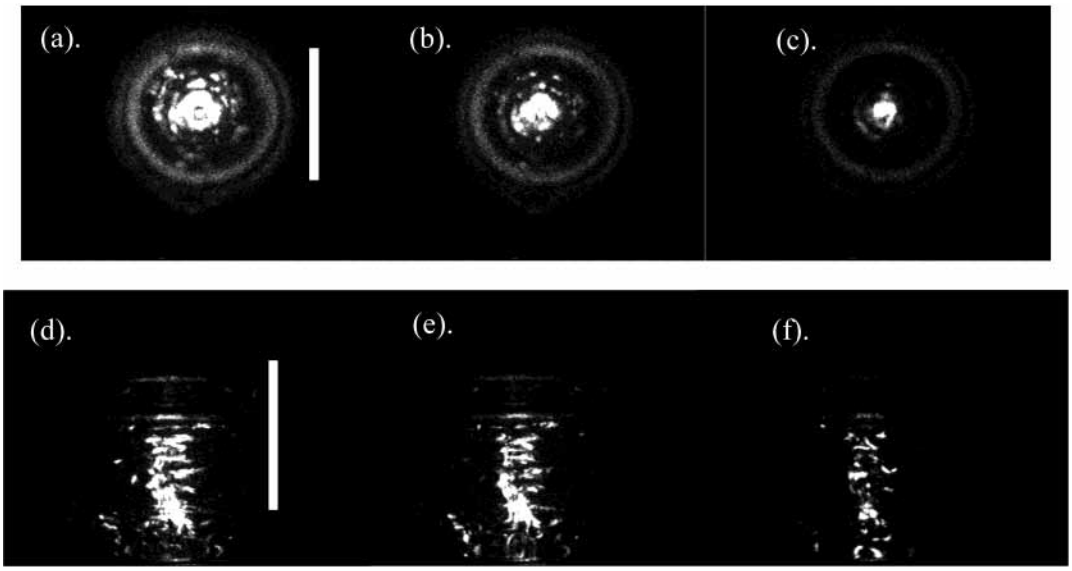

Figure 6. Frames showing the light emission from a cylindrical double-walled cell (5.8 cm internal diameter, 8.5 cm external diameter, and height 12 cm) recorded from above (frames a−c) and from the side (frames d−f). In all cases, the driving frequency was maintained at 120.15 kHz. The cell contained an aqueous solution identical to that reported in the legend of Figure 3. The cell was jacketed at 25 °C under aerobic conditions. The applied voltage was 107 V (2.15 bar) for frames a and d, 94 V (1.74 bar) for frames b and e, and 63 V (1.23 bar) for frames c and f. The scale bar in frame a represents 5.8 cm and applies to frames a−c while the scale bar in frame d represents 7.5 cm and applies to frames d−f. See parenthetical note in the Experimental Section.

Figure 5 shows the same cell under the same conditions of temperature and dimension driven at a slightly lower frequency (121.83 kHz). In this particular case, the mode appears to be (5,5,12). The assignment and measurement of the ring spacing are shown in Table 7. Again note that there is no central light spot in this case (see frame a). This indicates that a higher order mode ($m > 0$) was excited in the cell. The (4,5,12) mode is shown for comparison.

Figure 6 shows the same cell driven at 120.15 kHz. In this particular case, the mode appears to be (0,6,13). The assignment and measurement of the ring spacing are shown in Table 8.

In all of the measurements made, it appears that the speed of sound within the cavity is significantly reduced (in the range

TABLE 7: Measured and Predicted Ring Spacing for the Data Shown in Figure 5

	measured distance (cm)	predicted distance (cm)	predicted distance (cm)
ring 1	0.74 ± 0.2	0.9	0.8
ring 2	1.58 ± 0.2	1.50	1.4
ring 3	2.11 ± 0.2	1.95	1.9
ring 4	2.64 ± 0.2	2.45	2.4
m,n		5,5	4,5
$j_{m,n}$		20.58	19.20
$f_{m,n,12}^{\text{natural}}$ (kHz)[a]		210.54	201.54

[a] These values were calculated using the assignment system reported in Table 4 and a sound speed of 1500 m s^{-1}.

TABLE 8: Measured and Predicted Ring Spacing for the Data Shown in Figure 6

	measured distance (cm)	predicted distance (cm)
ring 1	0.63 ± 0.2	0.65
ring 2	1.31 ± 0.2	1.25
ring 3	1.84 ± 0.2	1.80
ring 4	2.37 ± 0.2	2.35
m,*n*		0,6
$j_{m,n}$		16.48
$f_{0,6,13}^{\text{natural}}$ (kHz)[a]		191.39

[a] These values were calculated using the assignment system reported in Table 4 and a sound speed of 1500 m s^{-1}.

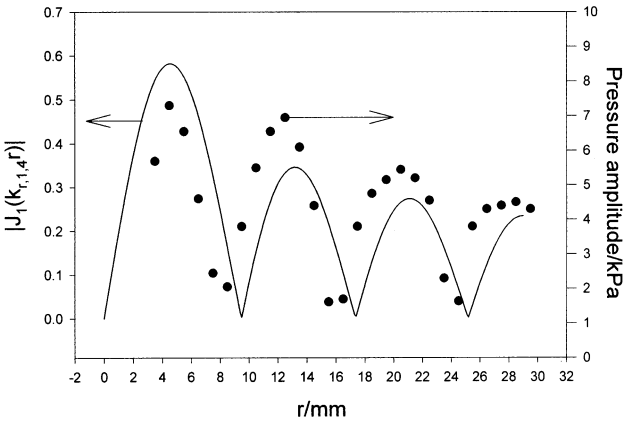

Figure 7. Plot showing the variation of the acoustic pressure amplitude (●) as a function of position as a hydrophone was scanned from the center of the cell to the wall. The solid line predicts the pressure profile for the (1,4,*q*) mode (i.e., resembling the magnitude of Figure 2a). A cylindrical double-walled cell (5.8 cm internal diameter, 8.5 cm external diameter, and height 12 cm) was employed containing 200 cm^3 50 mmol dm^{-3} Na_2SO_4. The experiment was performed under aerobic conditions at 25 °C. A sound frequency of 117.3 kHz was employed.

of 868−1063 m s^{-1}) when compared to bubble free media. This reduction in the effective speed of sound within the vessel in the presence of cavitation was further confirmed by measuring a number of modes at low driving pressures. The low driving pressure ensured that bubbles were not generated within the liquid hence enabling the bubble free sound speed to be determined. Figure 7 shows the response of a hydrophone measured as a function of radial position within the cell. The solid line on the figure represents the predicted pressure pattern for a (1,4,*q*) mode (i.e., resembling the magnitude of Figure 2a) in this particular case. It should be noted that in this experiment it is not the absolute pressure values that are important but the position and spacing of the pressure maxima and minima. Figure 7 shows that there is close agreement (±1.5 mm) between the measured spacing and the model. The spacing of the bands in the *z* direction was also measured, and from these two sets of data for a particular frequency, the mode

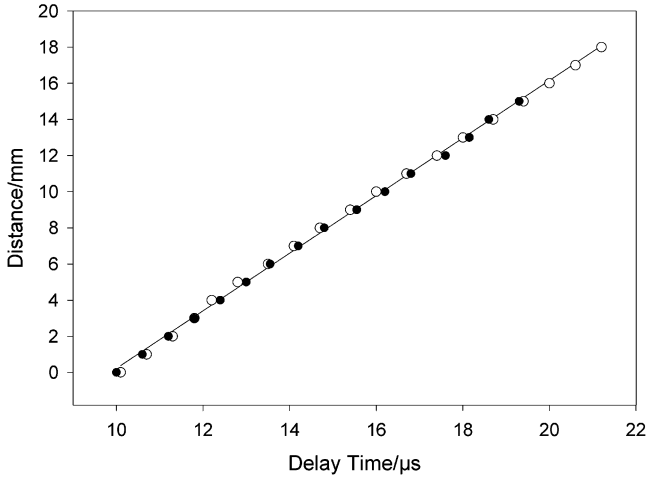

Figure 8. Plot showing the variation in the distance as a function of the delay time for a hydrophone placed centrally in a cylindrical cell (5.8 cm internal diameter, 8.5 cm external diameter, and height 12 cm). The cell contained 100 cm^3 50 mmol dm^{-3} Na_2SO_4 at 25 °C under either aerobic (●) or degassed, 0.22 μm filtered (○) conditions. A speed of sound of 1597 ± 25 m s^{-1} (95% confidence) was obtained.

assignment was determined. Table 9 shows a set of three frequencies with the measured spacing and predicted distances of both the ring-to-ring separation and band-to-band separation. To predict the mode frequency, it is necessary to determine the speed of sound within the bubble free environment. This sound speed measurement was achieved by measuring the "propagation delay", i.e., the time taken for an acoustic signal generated by the transducer to propagate a given distance to a hydrophone placed on-axis within the vessel. Because changes in the location of this axially positioned hydrophone can be measured to much greater accuracy than can the absolute distance over which the acoustic signal travels (which might also incur a systematic error), the sound speed was inferred from the gradient of plot of the arrival time of the start of the signal as the hydrophone was moved to a variety of on-axis locations. Figure 8 shows the propagation delay time measured in this manner plotted as a function of distance. Figure 8 clearly shows a linear dependence, as expected, and also indicates that full degassing of the liquid and filtering have no significant effects on the speed of sound within the media. This technique produced a speed of sound in a bubble free environment of 1597 ± 25 m s^{-1} (95% confidence interval). This value, when used with the model presented here, enabled the mode frequency to be calculated. Table 9 indicates that the predicted mode frequencies (assuming a rigid wall model; see Appendix A) and the actual mode frequencies are very similar. Clearly, this demonstrates that the model presented here is accurate supporting the assumptions made about the boundary conditions within the cavity.

It is in principle possible to invert measurements of the sound speed to obtain an estimation of the bubble population.[42]

TABLE 9: Measured Mode Assignment in the Absence of Cavitation[a]

experimental frequency (kHz)	104.3[c]	117.3	121.4
mode $j_{m,n,q}$	1,3,4	1,4,5	1,3,8
R_1-R_2 separation (mm) experimental	10.5 ± 1.5	7.0 ± 1.5	13.0 ± 1.5
R_1-R_2 separation (mm) theory	11.8	7.9	11.8
band separation (mm) theory	11	13.5	8.7
band separation (mm) experimental	11.3 ± 1.5	14.0 ± 1.5	8.0 ± 1.5
liquid height (mm)	51	74	74
f^{natural} (kHz) theory[b]	102.8	118.6	118.3

[a] R_1 and R_2 refer to the first and second rings in the radial direction. [b] Note that a speed of sound of 1597 m s^{-1} was employed and eq 13. The internal cell radius was $a = 2.9$ cm. The cell (glass double-walled) contained a 50 mmol dm^{-3} Na_2SO_4 solution, which was employed at 25 °C. [c] Solution degassed and filtered through a 0.22 μm filter. The errors shown are estimated from the size of the hydrophone employed.

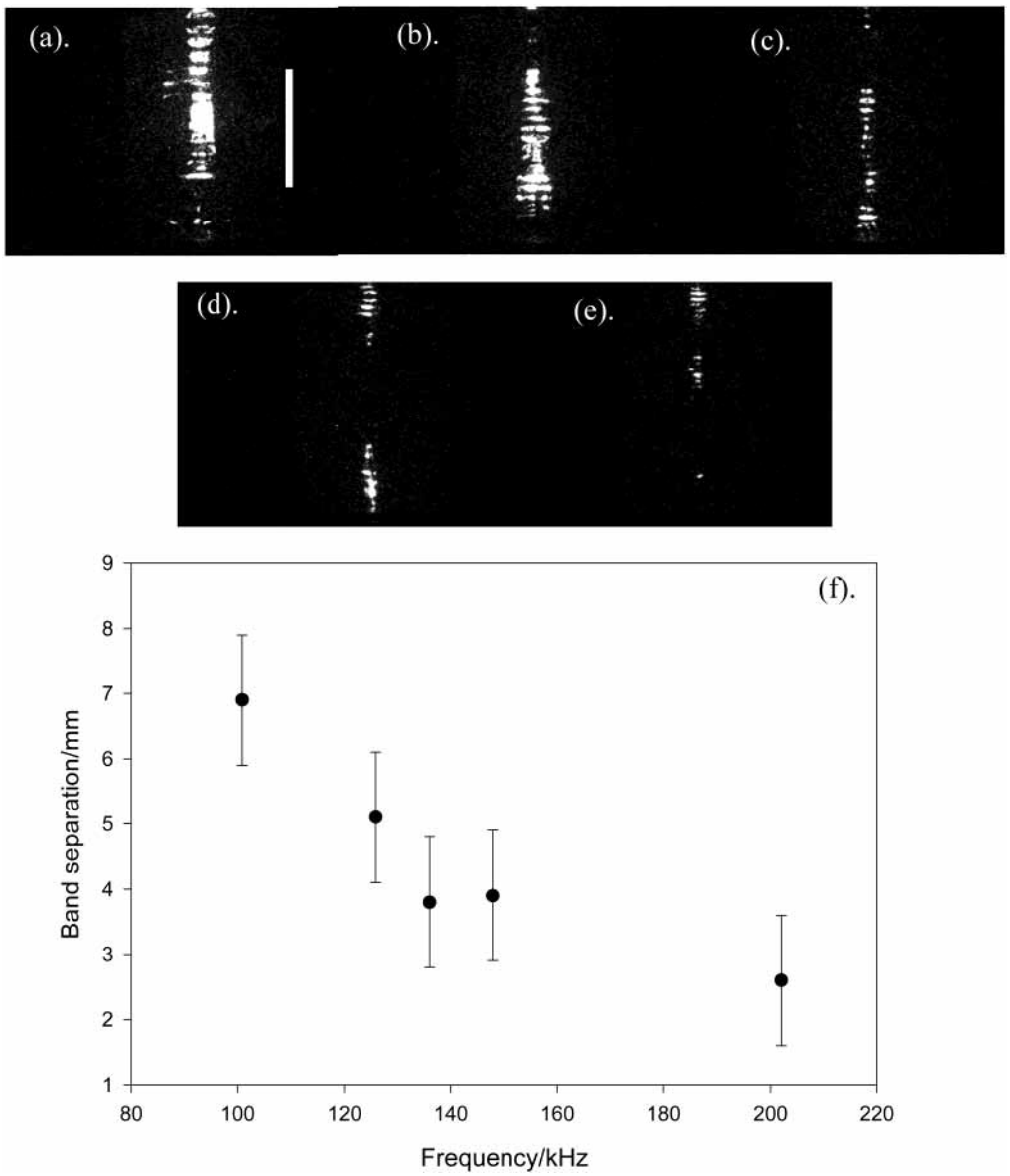

Figure 9. Frames showing the light emission from a cylindrical single-walled cell (9.4 cm internal diameter, 10 cm external diameter) recorded from the side. In all cases, the driving voltage was maintained at 90 V. The cell contained an aqueous solution identical to that reported in the legend of Figure 3. The pictures were recorded under ambient conditions (ca. 20−23 °C) in aerobic media. The solution height was maintained at 14 cm. The applied frequency was 100.87 kHz for frame a, 125.97 kHz for frame b, 147.83 kHz for frame c, 164.04 kHz for frame d, and 202 kHz for frame e. The scale bar in frame a represents 7 cm and applies to frames a−e. Frame f shows a plot of the band separation as a function of frequency.

However, this requires assumptions (free field conditions, bubble linearity, no interbubble interactions, etc.), which tend to become less valid the more complicated the sound field.[43] The bubble population under the cavitating conditions in this sonochemical reactor represents perhaps one of the most difficult circumstances in which this might be attempted, and indeed to our knowledge, it has not been tried before. The bubble population is inhomogeneous on an acoustically important spatial scale (for example, Bjerknes forces tending to force bubbles smaller than resonance to the pressure antinodes[44]); it will vary on time scales important to the measurement of the sound field (for example, bubbles pulsate with significant amplitude on the time scale of the acoustic period). However, the vessel itself has some characteristic sound speed, averaged in space and time, which controls the modal shapes and which is stable over the thousands of acoustic cycles over which a given mode can be continuously detected by its luminescence. Hence, a simple estimation of the void fraction (the proportion of volume present in the "bubbly liquid", which is gas/vapor rather than liquid) could be obtained using a Woods type equation. A key assumption for this to be valid would be that all of the bubbles present have equilibrium sizes smaller than that which would be resonant with the sound field.[44] While probably not true at all times, there is sufficient reasoning to suggest that this (rather than, say, the opposite) assumption would be a reasonable starting position. This is, first, because the bubbles, which emit luminescence from the pressure antinodes, will have equilibrium sizes smaller than resonance, because of Bjerknes forces.[44] Second, while in a cavitating sound field, bubble fragmentation and coalescence will occur, as the equilibrium size of a bubble increases so too does its tendency to be removed from the population by buoyancy or fragmentation (considering only the effect of surface tension and not the amplitude of pulsation of the wall and neglecting radiation forces). Hence, a reasonable starting position is the assumption that all of the bubbles present in the vessel have equilibrium sizes that are smaller than resonance. If this is the case, then

the sound speed is not dependent on the details of the bubble size distribution but on some "effective void fraction", VF. The latter represents the actual time- and space-dependent void fraction as some equivalent void fraction, which would be made up of smaller-than-resonance bubbles modeled as being uniformly distributed through the cylindrical resonator. The space- and time-averaged sound speed is therefore:[44]

$$c_c = c\{1 - (1/2)\,(VF)\,(\rho c^2/\kappa P_o)\} \qquad (14)$$

where c_c represents the reduced sound speed, κ is the polytropic index, and P_0 is the hydrostatic pressure. Employing appropriate values within eq 14 and sound speeds in the range of 868−1062 m s^{-1}, it is possible to calculate the void fractions within the cell to be $(2.9-4.2) \times 10^{-5}$. It is interesting to illustrate that if all of the bubbles were assumed to have a radius of 10 μm, a void fraction of 4.2×10^{-5} corresponds to a bubble population of 2×10^6 within the 200 cm^3 employed in the cell (see Figure 4). This corresponds to an average spacing of ca. 460 μm between each bubble. The Herring−Keller equation predicts that in a sound field of amplitude 3 bar (zero-to-peak), such a 10 μm radius bubble expands up to 56 μm and contracts to 0.5 μm in a 120 kHz sound field. All of the bubbles in this monodisperse population would pulsate in phase. As such, over each oscillatory cycle, the instantaneous void fraction in this idealized population would vary between 0.74% (at the moment when all of the bubbles were expanded) to 5.2×10^{-7}% (when all the bubbles are contracted). This vast range through which the cloud goes in a single oscillatory cycle is of course not going to be seen in a real polydisperse bubble cloud, where the oscillations are not in phase. However, it illustrates how remarkably robust are the space and time-averaged methods of the above paragraph (provided the assumptions inherent in the Woods type equation hold true), if the between tests variation in the inferred void fraction gives such a relatively small variation of $(2.9-4.2) \times 10^{-3}$%.

Given that the acoustics within the cell, and hence the particular mode, will be dependent on the bubble population through the apparent speed of sound, one can see that a mode once set up could detune through the generation of strong cavitation changing the speed of sound and hence the mode frequency. It is interesting, however, to speculate on the possibility that a mode will self-tune. As an example, if the bubble population is reduced in number because a mode detunes, then the speed of sound will change and in turn the mode frequency will change. Under the correct conditions, this could reexcite the original mode, hence increasing the bubble population, and so on. In this way, a particular mode could be very stable with respect to time. This observation is noted experimentally (see Figures 3−6). Indeed, the fact that a mode is stable over minutes despite the obvious effect of cavitation on the speed of sound suggests such a stabilizing mechanism or "bubble population feedback" must occur.

Figure 9 shows the effect of increasing the frequency on the band separation when the cell is viewed from the side. As the frequency raises, the band spaces concomitantly reduce (see Figure 9f). This is expected as the acoustic model predicts higher q values for higher driving frequency.

Figure 10 shows the effect of changing the solution height within the cell. As the solution height is progressively increased, it is clear that the pattern of bands (and hence the mode structure) changes within the cell. This can be clearly seen particularly through frames b−d. Frame c shows that under these conditions, even though the frequency and drive voltage remain the same, there is little or no cavitation activity. If the solution height is reduced or increased (see frames b and d, respectively), then a clear pattern reappears. Figure 10 clearly shows that the height of liquid is important in determining the cavitation activity within the reactor.

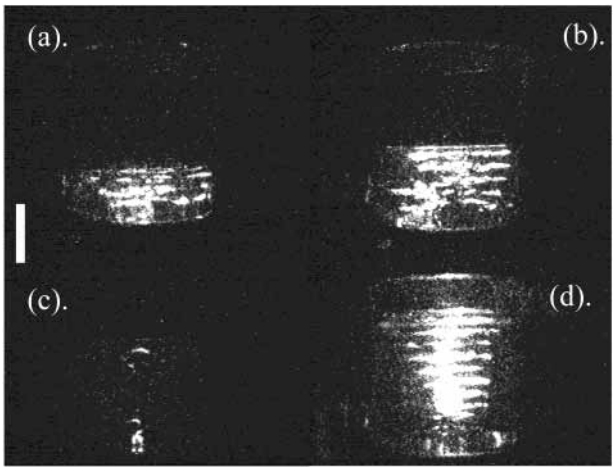

Figure 10. Frames showing the light emission from a cylindrical double-walled cell (5.8 cm internal diameter, 8.5 cm external diameter, and height 12 cm) recorded from the side. In all cases, the driving voltage was maintained at 130 V. The cell contained an aqueous solution identical to that reported in the legend of Figure 3. The cell was jacketed at 25 °C under aerobic conditions. The applied frequency was 104 kHz for all frames. In frame a, the solution height was 28 mm; frame b, 42 mm; frame c, 61 mm; and frame d, 80 mm. The scale bar represents 28 mm.

Figure 11 shows a progression of frames recorded as the drive frequency was increased from 116 to 131 kHz in 1 kHz steps. Figure 11 clearly shows that as the frequency was increased, the modal structure within the cell altered dramatically. This is demonstrated in frames f−h where in the space of a 2 kHz change in drive frequency (representing a 1.6% change) the modal pattern changes dramatically. Figure 11 shows that a relatively small change in the drive frequency can have dramatic effects on the cavitation activity within the cell.

The results presented in Figures 3−6 and 9−11 show that the definition of the bands within the cell changes as the acoustic pressure amplitude was varied. Indeed, some bands were no longer detectable at low driving pressures. However, this process may be the result of a number of factors. First, the detection system (e.g., the image-intensified camera) will have a critical light intensity below which a band will not be detected even though there is a pressure antinode in that position. Second, the critical pressure amplitude responsible for the light emission process imaged (e.g., the pressure amplitude for cavitation induced $OH^{\bullet}$ generation) is a complex matter relating cavitation bubble dynamics, bubble populations, and other physical parameters. Hence, considering these two points implies that the experimental determination of a band presence or absence through luminescent imaging is complex and may not be expected to be uniform throughout the cell. However, the model presented here does not attempt to predict the absolute pressure fluctuations (which can be measured using a hydrophone) but the position of the pressure antinodes and nodes, which can then be used to assign the mode. If all of the bands are not visible, it is still possible to assign the mode by measuring the band spacing where visible and using the relationship band spacing = liquid height/$(q + 0.5)$.

Consequences for Chemistry. If an ultrasonic cell of any particular geometry is used, the effects on chemistry will depend on the cell geometry, the frequency, the height of the solution, the material immersed within the solution, the construction of

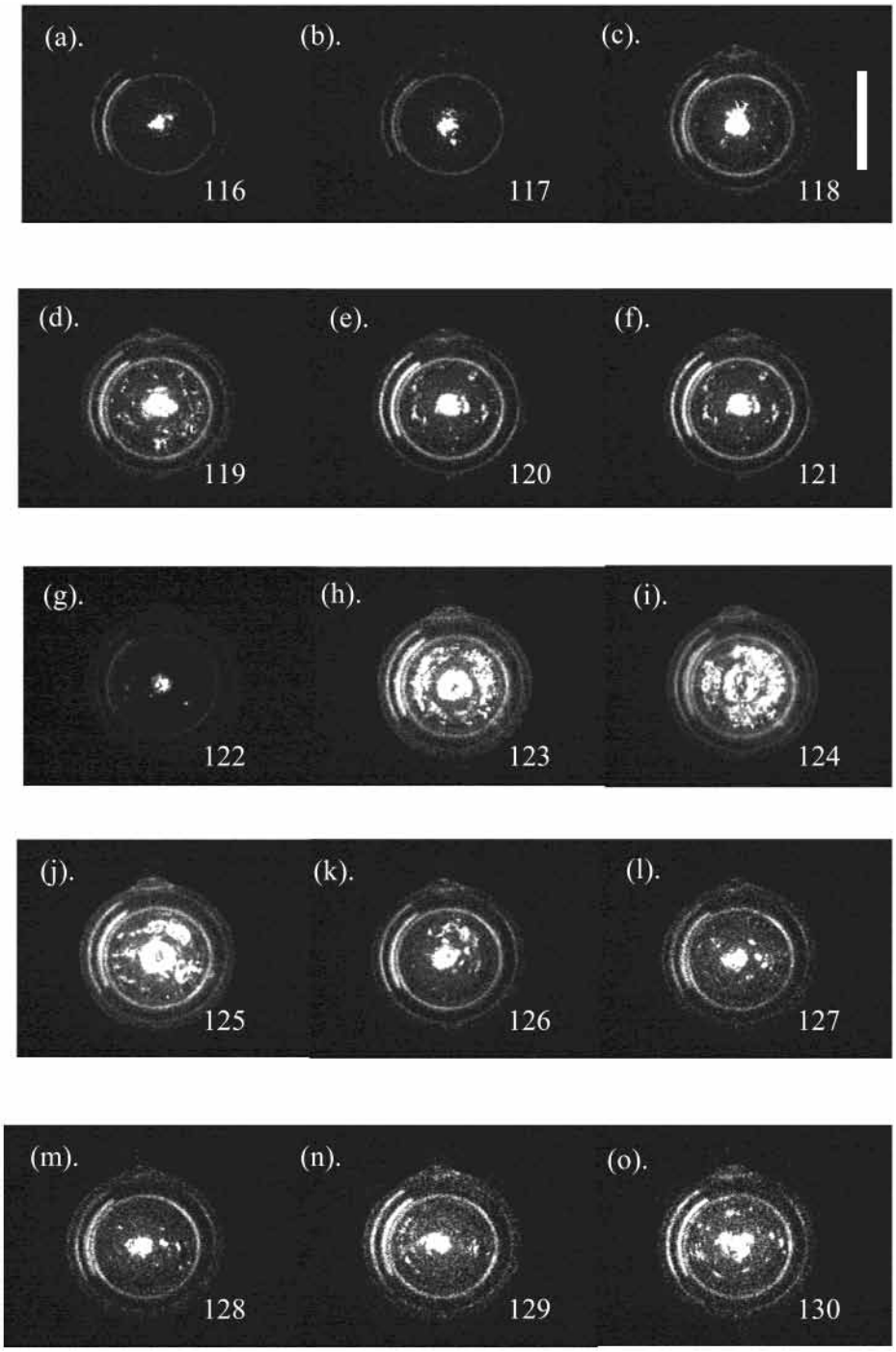

Figure 11. Frames showing the light emission from a cylindrical double-walled cell (5.8 cm internal diameter, 8.5 cm external diameter, and height 12 cm) recorded from above. The cell contained an aqueous solution identical to that reported in the legend of Figure 3. The cell was jacketed at 25 °C under aerobic conditions. The applied voltage was maintained at 95 V. The liquid height was 8 cm for all frames. The driving frequency was increased from 116 to 130 kHz in 1 kHz steps through frames a−o inclusively. The pressure amplitude over this range was 1.22, 1.41, 1.36, 1.38, 1.31, 1.39, 1.50, 1.80, 2.00, 1.76, 1.54, 1.42, 1.31, 1.33 and 1.26 bar, respectively. See parenthetical note in the Experimental Section. The scale bar represents 58 mm.

the cell walls, the bubble population, and the efficiency of the transducer at the frequency chosen. Even at a fixed frequency, with a given mode set up, the reading from a cavitation sensor (which may operate by detecting luminescence, erosion, sonochemistry, acoustic emission, etc.) will vary with its "footprint". Clearly, if the sensor is sufficiently small in size, the reading will be large if it is placed in a pressure antinode and small in a pressure node. If its footprint covers several antinode bands, then increasing the drive frequency will mean more bands of activity might be included in the sensors field of view, but each band will tend to be narrower than at lower frequency. Several reports exist documenting a change in the sonochemical activity as the frequency of ultrasound was increased in increments of tens or hundreds of kHz.[33,37,45−48] However, this may be a combination of effects. First, the modal pattern is more complex at higher frequencies; hence, more of the solution will be active. Second, it is unclear how the efficiency of radical production, considering the frequency dependence of the sound field, varies with the applied frequency. It must be pointed out that in most other studies the complex nature of the modal structure of the sound field has been overlooked. Indeed, this (and a companion paper, ref 49) are to

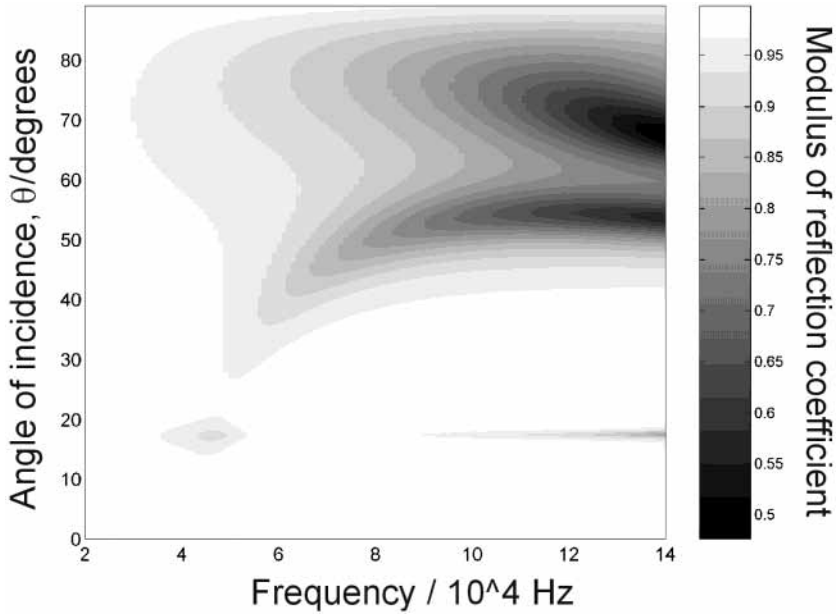

Figure 12. Plot showing the modulus of the reflection coefficient as a function of ultrasonic frequency and angle of incidence (θ). The acoustic model for the layered wall was solved as described in the text. The values of the parameters employed in the model were 1000 kg m^{-3} for the density of water, 1597 m s^{-1} for the speed of sound in the water phases, 2320 kg m^{-3} for the density of the glass used, 5640 m s^{-1} for the longitudinal wave speed of sound in the glass, 3280 m s^{-1} for the shear wave speed in the glass, 3.5 mm for the thickness of both glass layers, 6.5 mm for the separation of the glass layers comprising the water jacket, 1.2 kg m^{-3} for the density of air, and 345 m s^{-1} for the velocity of sound in the air phase.

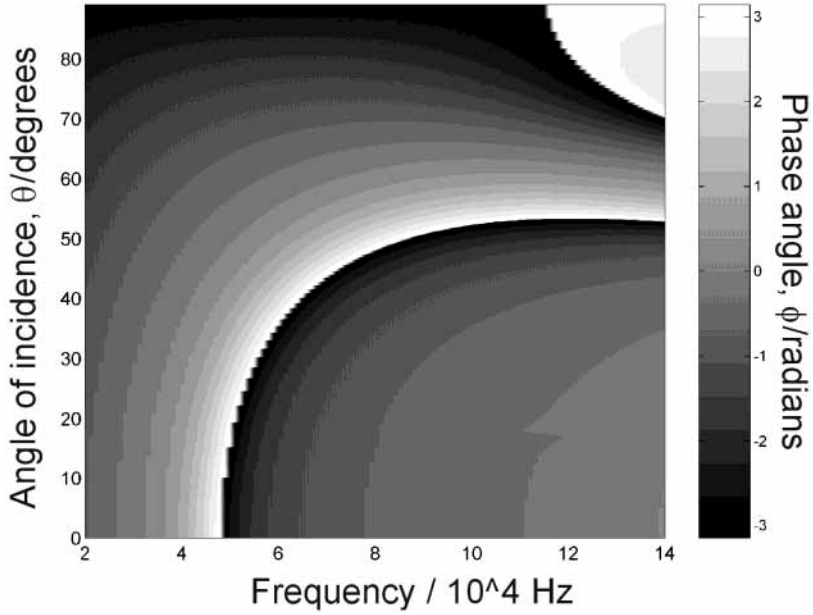

Figure 13. Plot showing the phase angle on reflection (ϕ) as a function of ultrasonic frequency and angle of incidence (θ). The acoustic model for the layered wall was solved as described in the text. The values of the parameters employed in the model were identical to those reported in Figure 12.

our knowledge the only sonochemical studies that have examined the frequency effect in 1 kHz increments. With this resolution, it is easy to see from Figure 11 that the sonochemiluminescence at times increases with frequency and at other times decreases with frequency. Yet, merely halving the resolution and increasing it in 2 kHz increments can suggest that luminescence decreases with frequency (e.g., if the luminescence was measured at 124, 126, and 128 kHz (Figure 11i,k,m, respectively)), or with a different starting frequency, increases with frequency (116, 118, and 120 kHz (Figure 11a,c,e)). Therefore, the practice of checking sonochemical activity at spot frequencies in reaction vessels can be entirely misleading, and trends may well be dominated by the frequency response of the transducer and the vessel, rather than of the cavitation chemistry.

It should be noted that this study indicates that it is important to consider the entire experimental arrangement employed in sonochemical experiments. This not only includes the drive electronics and transducer but the acoustic characteristics of the cell and the detection apparatus employed to determine the sonochemical effects. These considerations have rarely been applied, but discussion of it can be found in a companion paper in further detail.[49]

We are now in a position to reassess the findings of Trablesi et al.[22] and Compton et al.[23] In both cases, the mass transfer activity, which can be associated with cavitation activity within

the reactor, was investigated in cells with cylindrical geometries. Neither set of authors appealed to the Bessel function character of the acoustic modes in the vessel, which, as can be seen from this paper, explains both sets of results. The explanation for these findings proposed by Trablesi et al. was that in the center of the cell a "vaporlike" cavitation would exist. The observation of axisymmetric rings of activity is a clear result of the modal field, the presence or absence of a "central spot of activity" being dependent on the order of the Bessel function excited, and are not as a result of the type of cavitation events found within different parts of the cell.

Last, even though the modal functionality of a particular cell exhibits a large number of possible frequencies at which one may expect a standing wave pattern, it is important to remember that the efficiency of the driving signal, from in this case an ultrasonic transducer, will also be important. If, for example, a mode exists for the cavity but the efficiency of the transducer is low at that particular frequency, then the pressure field within the cell will also be of low amplitude. Alternatively, if the efficiency of the transducer is high (for example, at the transducer's resonant frequency) but a mode does not exist within the cavity, then only the material at the axis/focus of the cell might be treated. Only if the transducer is efficient and there is an appropriate mode at that particular frequency will there be a strong energy transfer from the transducer to the cell. This consideration is important in discerning why a particular cell will operate efficiently at some frequencies as compared to others for which it is thought that either the cell or the transducer is efficient. Clearly, this has consequences for the frequency dependence of a particular sonochemical reaction within a cell.[49]

There are two final points. First, at sufficiently high frequencies (> Schroeder frequency[50]), individual modes overlap and the modal nature of the sound field will disappear. Second, bubbles are not the only source of sound speed change. For every 1 °C rise in water temperature around room temperature, the sound speed (and hence the modal frequency) changes by 0.3%. Therefore, a 3 °C rise in temperature, which is not uncommon as a result of transducer heating in vessels (and is relied upon when calorific quantification of the transducer is measured[51]), which are not temperature-controlled, would be sufficient to cause the mode detuning seen in Figure 11 with similar major changes in reaction yield.

Conclusions

In the cell configuration, it was demonstrated that the activity of the solution was related to the modal sound field of the cavity. It is important to realize that unless the cell is driven below the first mode or above the Schroeder frequency,[50] the spatial variation in reaction (once a mode has been excited) and the frequency dependence of the yield (dictated by the frequency-dependent efficiency of the ultrasonic source, the modal acoustics of the cell, and possibly bubble dynamics) will be the key factors in determining the yield in all sonochemical reactors. It is concluded that the 3D geometry, frequency, reactor wall construction, transducer efficiency, temperature, and bubble population are all important factors in determining the effect of ultrasound on a particular system. It is anticipated that up to the Schroeder frequency, the frequency dependence of a reactor will follow a modal structure, as shown here, which can be modeled. The comparison between the model and the experimental results allows measurement of the reduction in sound speed within the cavity, which would be expected as the result of bubbles within the cavitating liquid. In addition, if the mode is measured within a cylindrical cell (in the absence of cavitation), the model can be used to determine the bubble free speed of sound.

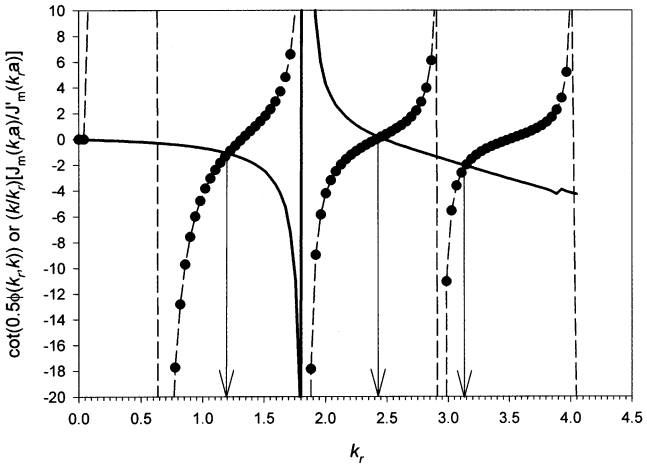

Figure 14. Plot showing the functions shown in eq A3 plotted as a function of k_r; ● represents the term containing the Bessel functions while − represents the cot term. The arrows show the crossing points. This plot was constructed considering a frequency of 117 kHz and a sound speed of 1597 m s^{-1}.

TABLE 10: Correction Caused by the Nonzero Phase Angle Determined from the Graphical Method Described in the Appendix[a]

experimental frequency (kHz)	k_r value at crossing points	natural frequency at k_r (kHz)
104	$k_{r1} = 1.20$	76.8
	$k_{r2} = 2.43$	93.4
	$k_{r3} = 3.24$	**108.4**
117	$k_{r1} = 1.25$	67.3
	$k_{r2} = 1.97$	77.6
	$k_{r3} = 2.505$	97.0
	$k_{r4} = 43.2$	100.7
	$k_{r5} = 4.25$	**123.3**
121	$k_{r1} = 1.30$	97.5
	$k_{r2} = 2.05$	105.5
	$k_{r3} = 2.6$	113
	$k_{r4} = 3.225$	**123**
	$k_{r5} = 4.15$	139.8

[a] The numbers in bold represent the likely natural frequency of the cell.

The modeling of the acoustics within the cylindrical chamber indicates that the inner wall can be considered as largely reflecting. However, the phase angle on reflection at the inner wall is nonzero. Nevertheless, the correction to the natural frequency of the cavity due to this complication is small (ca. <5.5%) and to a first approximation can be ignored.

Last, small changes in the physical conditions, such as temperature,[51] solution volume, wall materials, and construction or frequency (of the order of 1−2%) can have dramatic effects on the experimental observations and ultimately the conclusions drawn from the study.

Acknowledgment. We thank the EPSRC (Grant GR/M24615) for funding. T.G.L. is grateful to the Royal Society Leverhulme Trust Senior Research Fellowship scheme for support.

Appendix A

An acoustic model was used to determine the reflection coefficient and phase angle upon reflection at the discretely layered boundary presented by the inner cell wall. While this

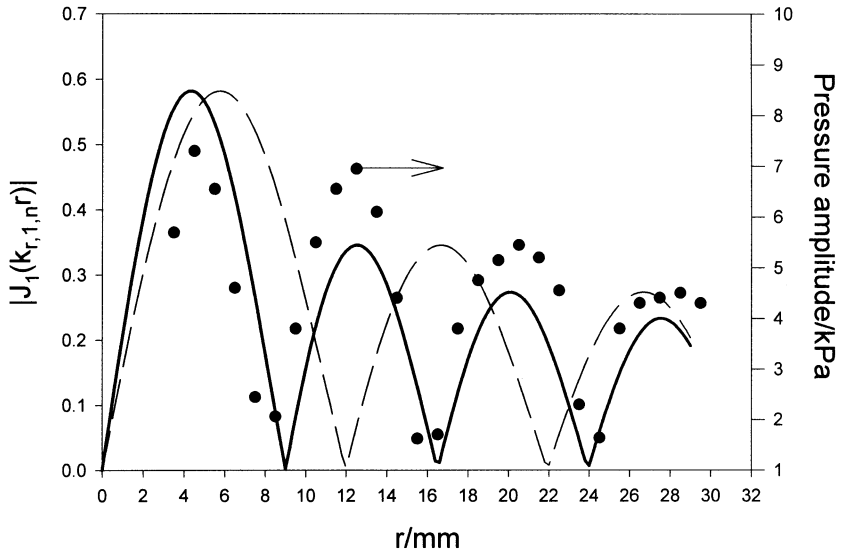

Figure 15. Plot showing the predicted variation of the pressure field plotted as a function of distance for k_{14} (− −) and k_{15} (−). The actual measured pressure is also shown (●). The experimental conditions are reported in Figure 7.

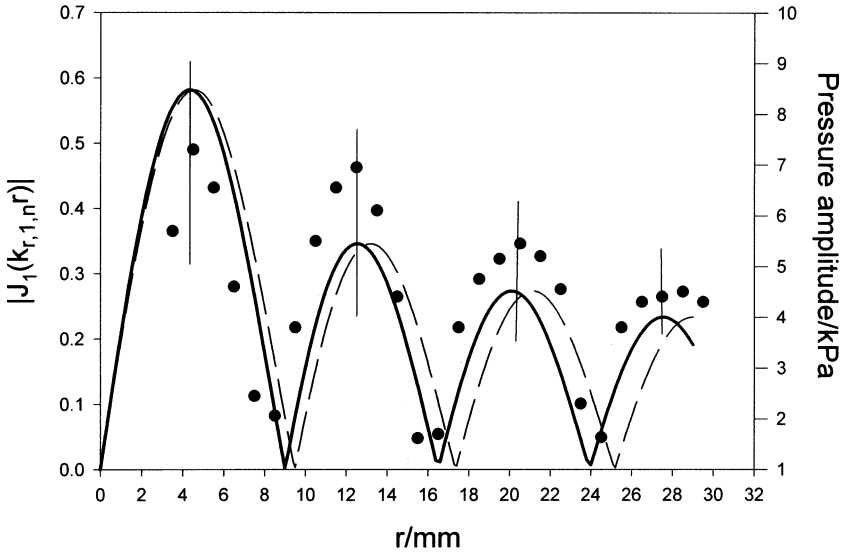

Figure 16. Plot showing the predicted variation of the pressure field plotted as a function of distance for the soft wall model k_{15} (−) and the hard wall model (− −). The actual measured pressure is also shown (●). The vertical lines are illustrative of the improved agreement between theory and experiment. The experimental conditions are reported in Figure 7.

approach in calculating the boundary conditions at the walls of the vessel is not unique for layered media in sediment acoustics,[52] this is the first time, to the knowledge of the authors, that it has been performed for the boundary conditions of a sonochemical cell. The modeling was achieved using MATLAB following a reported method that can be found elsewhere.[53]

Figure 12 shows the reflection coefficient at the inner wall of the cell plotted as a function of acoustic drive frequency and angle of incidence (θ). Figure 12 shows that for the majority of the incidence angle/frequency space, the magnitude of the reflection coefficient is close to 1. This indicates that the inner interface at the cell wall can be considered as highly reflecting with the energy of the acoustic wave "trapped" within the inner cylindrical cavity. Figure 13 shows the associated phase angle (ϕ) on reflection at the inner wall. It is apparent from this figure that the phase angle is neither zero nor 2π over the incidence angle/frequency space considered. This implies that the inner wall cannot be truly considered as rigid. However, it is possible to calculate the effect of this nonrigid boundary on the natural frequencies of the cavity.

Assuming unity reflection coefficient, the complex reflection coefficient at the cylinder wall may be written as

$$R(\omega,\theta) = e^{i\phi(\omega,\theta)}$$

The equivalent, locally reacting impedance at the wall is then given as

$$Z(\omega,\theta)/\rho c = (1 + e^{i\phi})/(1 - e^{i\phi})$$

which simplifies to

$$Z(\omega,\theta)/\rho c = i \cot(\phi(\omega,\theta)/2) \qquad \text{(A1)}$$

at $r = a$. In the absence of energy loss at the cylinder wall, we assume solutions in the radial direction of the form of $p \propto J_m(k_{mn}r)$, whose impedance is given by

$$Z/\rho c = i\,(k/k_{rmn})\,[J_m(k_{rmn}a)/J_m'(k_{rmn}a)] \qquad \text{(A2)}$$

where J_m' represents the derivative with respect to the argument. Equating A1 and A2 yields the following transcendental

equation for the radial wavenumbers k_{rmn}

$$(k/k_{rmn})\,[J_m(k_{rmn}a)/J_m'(k_{rmn}a)] = \cot(\phi(k_{rmn},k)/2) \quad \text{(A3)}$$

where $\phi(\omega,\theta)$ has been expressed as a function of wavenumbers, $\phi(k_{rmn},k)$. Equation A3 was solved graphically. Figure 14 shows the functions in eq A3 plotted as a function of k_{rmn} for 117 kHz (see Table 9). The crossing points of the two functions give values of k_{rmn} that are solutions of eq A3. Table 10 shows a collection of the k_{rmn} values obtained using this method and their associated natural frequencies. To determine which value of k_{rmn} is required to calculate the natural frequency of the cavity, it is illustrative to compare the pressure distance data shown in Figure 7 with the predicted dependence from the theory. This comparison is shown in Figure 15 for $k_{r,1,4}$ and $k_{r,1,5}$. Figure 15 clearly shows that the $k_{r,1,5}$ value is appropriate for this example. It is also interesting to compare the soft wall model described here in detail with the hard wall assumption shown in the main text. Figure 16 shows the comparison of the $k_{r,1,5}$ function as compared to the pressure distance dependence determined from counting the rings in Figure 7 and using the hard wall approximation. Figure 7 shows that although the soft wall model ($k_{r,1,5}$) is the most accurate at predicting the position of the pressure maxima and the slight down turn in the pressure amplitude at the wall ($r = 2.9$ cm), the hard wall model (dashed line) is still reasonably good. In turn, if we consider the prediction of the natural frequencies of the modes reported in Tables 9 (hard wall) and 10, it is clear that the discrepancy between the hard wall and the soft wall models in comparison with the experimental data is small. Indeed, a maximum error of 5.4% was found for these measurements in comparison to theory. The modification of the natural frequency of the cell is relatively small and cannot explain the variation in the speed of sound in the cavity determined from the luminescent pictures shown in the results section. It is also important to note that the soft wall approach described here cannot be applied to the cavitation experiments (see Figures 3−6) as the model requires a prior knowledge of the speed of sound within the cell (e.g., to calculate the k value). In this instance, the hard wall model has to be adopted. However, the error in this approach is small (ca. 5%) and cannot explain the difference in the sound speeds observed (up to ca. 46%) in the presence of cavitation, which we attribute to bubbles (see main text).

References and Notes

(1) Price, G. J.; West, P. J.; Smith, P. F. *Ultrason. Sonochem.* **1994**, *1*, s51−s57.

(2) Suslick, K. S.; Hammerton, D. A.; Cline, R. E. *J. Am. Chem. Soc.* **1986**, *108*, 5641−5642.

(3) Suslick, K. S.; Goodale, J. W.; Wang, H. H.; Schubert, P. F. *J. Am. Chem. Soc*. **1983**, *105*, 5781−5785.

(4) Suslick, K. S.; Didenko, Y.; Fang, M. M.; Hyeon, T.; Holneck, K. J.; McNamara, W. B.; Mdleleni, M. M.; Wong, M. *Philos. Trans. R. Soc. London, Ser. A* **1999**, *357*, 335−353.

(5) Portenlanger, G.; Heusinger, H. *Ultrason. Sonochem*. **1997**, *4*, 127−130.

(6) Pickworth, M. J. W.; Dendy, P. P.; Twentyman, P. R.; Leighton, T. G. *Phys. Med. Biol.* **1989**, *34*, 1553−1560.

(7) Mason, T. J. *Chem. Ind.* **1993**, *Jan*, 47−50.

(8) Chendke, P. K.; Fogler, H. S. *Ultrasonics* **1975**, *13*, 31−37.

(9) Colussi, A. J.; Hung, H. M.; Hoffmann, M. R. *J. Phys. Chem. A* **1999**, *103*, 2696−2699.

(10) Hoffmann, M. R.; Hua, I.; Hochemer, R. *Ultrason. Sonochem.* **1996**, *3*, S163−S172.

(11) Suslick, K. S.; Mdleleni, M. M.; Ries, J. T. *J. Am. Chem. Soc*. **1997**, *119*, 9303−9304.

(12) Madigan, N. A.; Coury, L. A. *Anal. Chem.* **1997**, *69*, 5−15. (b) Zhang, H.; Coury, L. A. *Anal. Chem.* **1993**, *65*, 1552−1558.

(13) Marken, F.; Eklund, J. C.; Compton, R. G. *J. Electroanal. Chem.* **1995**, *395*, 335−339.

(14) Agra-Gutierrez, C.; Compton, R. G. *Electroanalysis* **1998**, *10*, 204−206. (b) Agra-Gutierrez, C.; Compton, R. G. *Electroanalysis* **1998**, *10*, 603−612. (c) Akkermans, R. P.; Ball, J. C.; Rebbitt, T. O.; Marken, F.; Compton, R. G. *Electrochim. Acta* **1998**, *43*, 3443−3449. (d) Agra-Gutierrez, C.; Hardcastle, J. L.; Ball, J. C.; Compton, R. G. *Analyst* **1999**, *124*, 1053−1057. (e) Davis, J.; Compton, R. G. *Anal. Chim. Acta* **2000**, *404*, 241−247.

(15) Birkin, P. R.; Silva-Martinez, S. *J. Chem. Soc. Chem. Commun.* **1995**, 1807−1808. (b) Birkin, P. R.; Silva-Martinez, S. *J. Electroanal. Chem.* **1996**, *416*, 127−138. (c) Birkin, P. R.; O'Connor, R.; Rapple, C.; Silva-Martinez, S. *J. Faraday Trans.* **1998**, *94*, 3365−3371.

(16) Bard, A. J. *Anal. Chem*. **1963**, *35*, 1125−1128.

(17) Perusich, S. A.; Alkire, R. C. *J. Electrochem. Soc.* **1991**, *138*, 700−707. (b) Perusich, S. A.; Alkire, R. C. *J. Electrochem. Soc.* **1991**, *138*, 708−713.

(18) Dewald, H. D.; Peterson, B. A. *Anal. Chem*. **1990**, *62*, 779−782.

(19) Atobe, M.; Matsuda, K.; Nonaka, T. *Electronalysis* **1996**, *8*, 784−788.

(20) Walton, D. J.; Burke, L. D.; Murphy, M. M. *Electrochim. Acta* **1996**, *41*, 2747−2751.

(21) Birkin, P. R.; Leighton, T. G.; Simpson, M. D.; Offin, D. Manuscript in preparation.

(22) Trabelsi, T.; Ait-lyazidi, H.; Berlan, J.; Fabre, P. L.; Delmas, H.; Wilhelm, A. M. *Ultrason. Sonochem.* **1996**, *6*, s125−s130.

(23) Javier Del Campo, F.; Coles, B. A.; Marken, F.; Compton, R. G.; Cordemans, E. *Ultrason. Sonochem.* **1999**, *6*, 189−197.

(24) Neppiras, E. A. *Phys. Rep.* **1980**, *61*, 159−251.

(25) Mettin, R.; Luther, S.; Ohl, C.-D.; Lauterborn, W. *Ultrason. Sonochem*. **1999**, *6*, 25−29.

(26) Crum, L. A.; Reynolds, G. T. *J. Acoust. Soc. Am*. **1985**, *78*, 137−139.

(27) Birkin, P. R.; Leighton, T. G.; Watson, Y. E.; Power, J. F. *Acoust. Bull.* **2001**, *Sept/Oct*, 24−37.

(28) Birkin, P. R.; Bowen, C. R.; Delaplace, C. L. *J. Phys. Chem. B* **1998**, *102*, 10885−10893.

(29) Gundermann, K. D. *Chemiluminescence in Organic Chemistry*; Springer-Verlag: Berlin, 1987.

(30) Merenyi, G.; Lind, J. S. *J. Am. Chem. Soc.* **1980**, *102*, 5831−5835. (b) Lind, J.; Merenyi, G.; Eriksen, T. E. *J. Am. Chem. Soc.* **1983**, *105*, 7655−7661.

(31) McMurray, H. N.; Wilson, B. P. *J. Phys. Chem. A* **1999**, *103*, 3955−3962.

(32) Negishi, K. *J. Phys. Soc. Jpn.* **1961**, *16*, 1450−1465.

(33) Mark, G.; Tauber, A.; Laupert, R.; Schuchmann, H. P.; Schulz, D.; Mues, A.; von Sonntag, C. *Ultrason. Sonochem*. **1998**, *5*, 41−52.

(34) Weissler, A.; Copper, H. W.; Snyder, S. *J. Am. Chem. Soc.* **1950**, *72*, 1769−1775.

(35) Price, G. J.; Lenz, E. J. *Ultrasonics* **1993**, *31*, 451−456.

(36) Hart, E. J.; Henglein, A. *J. Phys. Chem.* **1987**, *91*, 3654. (b) Hart, E. J.; Henglein, A. *J. Phys. Chem*. **1985**, *89*, 4342.

(37) Henglein, A. *Ultrason. Sonochem*. **1995**, *2*, S115−S121.

(38) Kinsler, L. E.; Frey, A. R.; Coppens, A. B.; Sanders, J. V. *Fundamentals of Acoustics*, 3rd ed; John Wiley & Sons: New York, 1982.

(39) Information supplied by Morgan Electro Ceramics.

(40) Reynolds, D. D. *Engineering Principles of Acoustics*; Allyn & Bacon: Boston, 1981.

(41) Fox, F. E.; Curley, S. R.; Larson, G. S. *J. Acoust. Soc. Am.* **1955**, *27*, 534−539.

(42) Commander, K. W.; McDonald, R. J. *J. Acoust. Soc. Am.* **1991**, *89*, 592−597.

(43) Meers, S. D.; Leighton, T. G.; Clarke, J. W. L.; Heald, G. J.; Dumbrell, H. A.; White, P. R. Acoustical Oceanography. In *Proceedings of the Institute of Acoustics*; Leighton, T. G., Heald, G. J., Griffiths, H., Griffiths, G., Eds.; Institute of Acoustics, Bath University Press: Bath, 2001; Vol. 23, Part 2, pp 235−241.

(44) Leighton, T. G. *The Acoustic Bubble*; Academic Press: London, 1994.

(45) Hung, H.; Hoffmann, M. R. *J. Phys. Chem. A* **1999**, *103*, 2734−2739.

(46) Kojima, Y.; Koda, S.; Nomura, H. *Ultrason. Sonochem*. **2001**, *8*, 75−79.

(47) Sato, M.; Itoh, H.; Fujii, T. *Ultrasonics* **2000**, *38*, 312−215.

(48) Becket, M. A.; Hua, I. *J. Phys. Chem. A* **2001**, *105*, 3796−3802.

(49) Birkin, P. R.; Power, J. F.; Vinçotte, A. M. L.; Leighton, T. G. Submitted for publication.

(50) Fahy, F. J. *Foundations in Engineering Acoustics*; Academic Press: London, 2001; pp 256−262.

(51) Mason, T. J.; Lorimer, J. P.; Bates, D. M. *Ultrasonics* **1992**, *30*, 40−42.

(52) Brekhovskikh, L. M. *Waves in Layered Media*; Academic Press: New York, 1960.

(53) Cervenka, P.; Challande, P. *J. Acoust. Soc. Am.* **1991**, *89*, 1579−1589.